Calcium modulates the domain flexibility and function of an α-actinin similar to the ancestral α-actinin

Nikos Pinotsis[a,1,2], Karolina Zielinska[a,1,3], Mrigya Babuta[b,1,4], Joan L. Arolas[a,1], Julius Kostan[a], Muhammad Bashir Khan[a,5], Claudia Schreiner[a], Anita Salmazo[a,6], Luciano Ciccarelli[c,d,e,f,g], Martin Puchinger[a], Eirini A. Gkougkoulia[a], Euripedes de Almeida Ribeiro Jr[a,7], Thomas C. Marlovits[c,d,e,f,g], Alok Bhattacharya[b,8], and Kristina Djinovic-Carugo[a,h,9]

[a]Department of Structural and Computational Biology, Max Perutz Labs, University of Vienna, A-1030 Vienna, Austria; [b]School of Life Sciences, Jawaharlal Nehru University, 110067 New Delhi, India; [c]Centre for Structural Systems Biology, D-22607 Hamburg, Germany; [d]Institute for Structure and Systems Biology, University Medical Center Hamburg-Eppendorf, D-20246 Hamburg, Germany; [e]Deutsches Elektronen-Synchrotron, D-22607 Hamburg, Germany; [f]Institute of Molecular Biotechnology, Austrian Academy of Sciences, A-1030 Vienna, Austria; [g]Research Institute of Molecular Pathology, A-1030 Vienna, Austria; and [h]Department of Biochemistry, Faculty of Chemistry and Chemical Technology, University of Ljubljana, SI-1000 Ljubljana, Slovenia

Edited by Thomas D. Pollard, Yale University, New Haven, CT, and approved July 29, 2020 (received for review October 15, 2019)

The actin cytoskeleton, a dynamic network of actin filaments and associated F-actin–binding proteins, is fundamentally important in eukaryotes. α-Actinins are major F-actin bundlers that are inhibited by Ca^{2+} in nonmuscle cells. Here we report the mechanism of Ca^{2+}-mediated regulation of *Entamoeba histolytica* α-actinin-2 (*Eh*Actn2) with features expected for the common ancestor of *Entamoeba* and higher eukaryotic α-actinins. Crystal structures of Ca^{2+}-free and Ca^{2+}-bound *Eh*Actn2 reveal a calmodulin-like domain (CaMD) uniquely inserted within the rod domain. Integrative studies reveal an exceptionally high affinity of the *Eh*Actn2 CaMD for Ca^{2+}, binding of which can only be regulated in the presence of physiological concentrations of Mg^{2+}. Ca^{2+} binding triggers an increase in protein multidomain rigidity, reducing conformational flexibility of F-actin–binding domains via interdomain cross-talk and consequently inhibiting F-actin bundling. In vivo studies uncover that *Eh*Actn2 plays an important role in phagocytic cup formation and might constitute a new drug target for amoebic dysentery.

α-actinin | F-actin bundling and binding | calcium regulation | modulation of structural rigidity | crystal structure

The actin cytoskeleton may have been key for the development of fundamental early eukaryotic processes such as cytokinesis and phagocytosis. Effective actin-based force generation requires the presence of actin-binding proteins (ABPs) to both cross-link or bundle actin filaments (F-actin) and anchor them to membranes and other subcellular structures. α-Actinin is a major F-actin–bundling protein that belongs to the spectrin superfamily and is found in most organisms apart from plants and prokaryotes (1, 2). α-Actinin achieves bundling via an antiparallel dimeric topology in which each subunit comprises an N-terminal F-actin–binding domain (ABD), a connecting segment (neck), a central rod domain built by spectrin-like repeats (SRs), and a C-terminal calmodulin-like domain (CaMD) comprising four EF-hand motifs composed of two lobes (EF1-2 and EF3-4) (Fig. 1*A*). In humans, α-actinin isoforms 2 and 3 are Ca^{2+}-insensitive and key players in the function of striated muscle, where they are regulated by phosphoinositides (3–5). By contrast, isoforms 1 and 4 are Ca^{2+}-sensitive and widely expressed in most nonmuscle cell types (6, 7). F-actin bundles formed by nonmuscle α-actinins function as scaffolds that support or stabilize cellular structures such as focal adhesion contacts, cell protrusions, and stress fibers (2, 7, 8). F-actin–bundling activity of nonmuscle α-actinins is inhibited by Ca^{2+} concentrations higher than 0.1 mM (9, 10), but the mechanism behind this regulation is unknown (11).

Intragenic duplication that occurred in ancient organisms somewhere between the common ancestor of amoeba/fungus/animal and animal α-actinins (with one/two SRs) has given rise to the more complex forms (with four SRs) found in higher eukaryotes (12, 13) (Fig. 1 *A* and *B*). *Entamoeba histolytica*, the etiological agent of amoebic dysentery (also known as amoebiasis), is an anaerobic protozoan that infects predominantly humans and is responsible for 40,000 to 110,000 deaths a year, most of them in developing countries (14, 15). The life cycle and pathogenesis of *E. histolytica* rely on phagocytosis, which requires a dramatic reorganization of the parasite cytoskeleton during phagocytic cup formation as well as phagosome formation and maturation (16–18). Ca^{2+} plays an important role during different steps of *E. histolytica* phagocytosis such as phagosome closure and maturation

Significance

Actin is one of the most abundant proteins in eukaryotic cells. Actin filaments together with a large number of actin-binding proteins are critical players in many cellular functions, ranging from cell motility and muscle contraction to maintenance of cell shape and transcription regulation. α-Actinin—a member of the spectrin superfamily—is an archetypical F-actin–binding and –bundling protein. It is known that Ca^{2+} inhibits α-actinin capacity to bundle F-actin. We present a structure of a Ca^{2+}-regulated α-actinin and propose the mechanism for its regulation. We uncover that Ca^{2+} binding triggers an increase in protein rigidity, leading to reduced conformational flexibility and bundling activity. The proposed molecular mechanism is likely to be a blueprint for regulation of spectrin-like proteins.

Author contributions: N.P., K.Z., J.L.A., J.K., T.C.M., A.B., and K.D.-C. designed research; N.P., K.Z., M.B., J.L.A., J.K., M.B.K., C.S., A.S., L.C., M.P., E.A.G., and E.d.A.R. performed research; N.P., K.Z., M.B., J.L.A., J.K., M.B.K., M.P., E.A.G., E.d.A.R., and K.D.-C. analyzed data; and N.P., M.B., J.L.A., J.K., and K.D.-C. wrote the paper.

The authors declare no competing interest.

This article is a PNAS Direct Submission.

[1]N.P., K.Z., M.B., and J.L.A. contributed equally to this work.

[2]Present address: Institute of Structural and Molecular Biology, Department of Biological Sciences, Birkbeck College, WC1E 7HX London, United Kingdom.

[3]Present address: Novartis Institutes for BioMedical Research, Novartis, 6250 Kundl, Austria.

[4]Present address: Division of Gastroenterology, Department of Medicine, Center for Life Science, Beth Israel Deaconess Medical Center, Boston, MA 02115.

[5]Present address: Department of Biochemistry, University of Alberta, Edmonton, AB T6G 2H7, Canada.

[6]Present address: Institute of Science and Technology Austria, 3400 Klosterneuburg, Austria.

[7]Present address: Pharmaceutical Science and Devices, Plasma-derived Therapies, R&D, Takeda Pharmaceutical Company Ltd., A-1220 Vienna, Austria.

[8]Present address: Department of Biology, Ashoka University, Sonepat, 131029 Haryana, India.

[9]To whom correspondence may be addressed. Email: kristina.djinovic@univie.ac.at.

This article contains supporting information online at https://www.pnas.org/lookup/suppl/doi:10.1073/pnas.1917269117/-/DCSupplemental.

First published August 26, 2020.

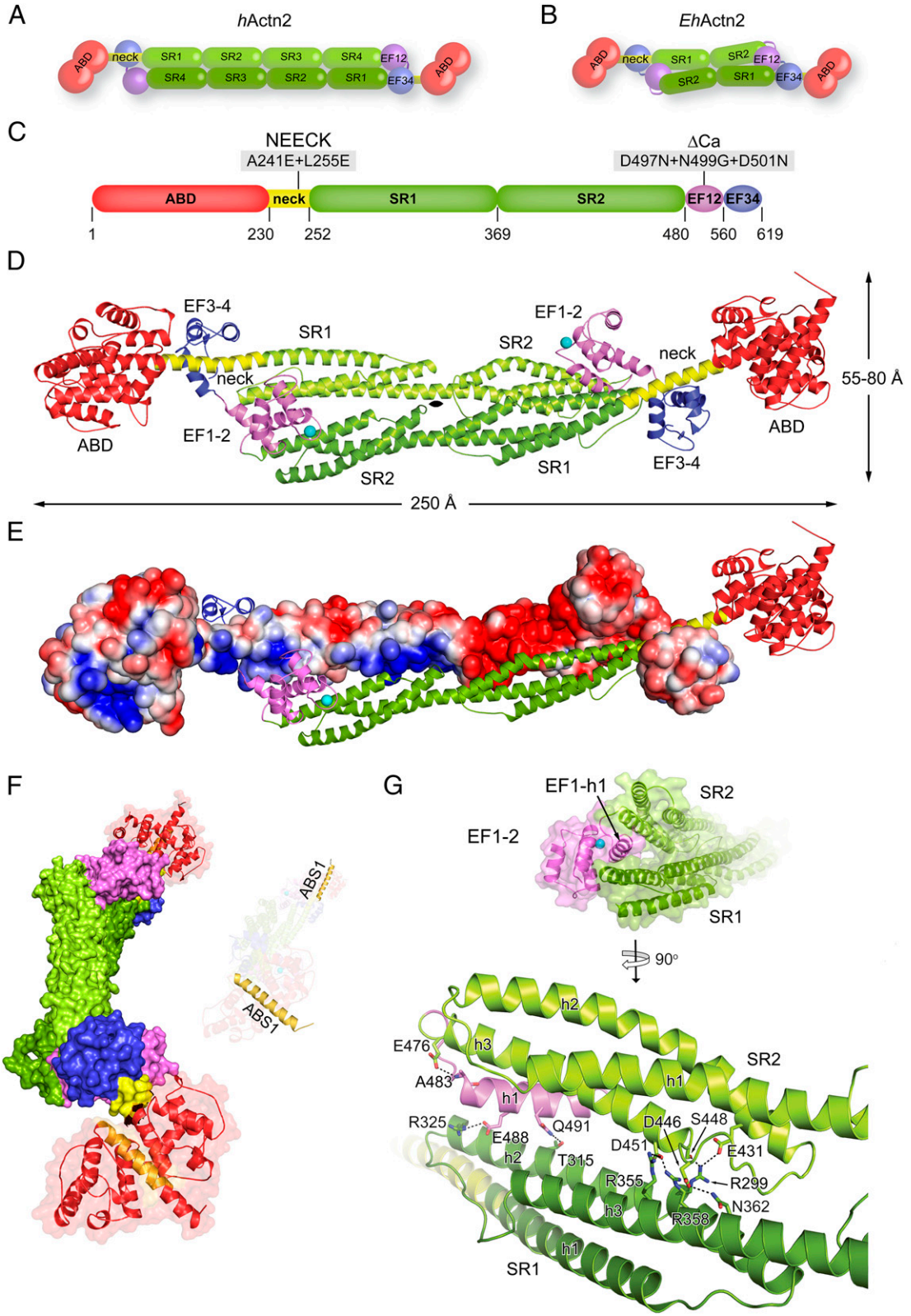

Fig. 1. *Eh*Actn2 structure reveals a unique multidomain architecture. (*A*) Domain composition of the *h*Actn2 dimer showing the ABD (red), neck (yellow), rod (composed of SR1 to SR4; green), EF1-2 (violet), and EF3-4 (blue). (*B*) Domain composition of the *Eh*Actn2 dimer (color-coded as in *A*). (*C*) Domain boundaries of the *Eh*Actn2 sequence from UniProt (UP) code C4LWU6. Mutations on the NEECK and ΔCa constructs are indicated. (*D*) Structure of Ca^{2+}-bound *Eh*Actn2 shown in a ribbon representation (color-coded as in *A*). Ca^{2+} is shown as a cyan sphere. (*E*) Structure of Ca^{2+}-bound *Eh*Actn2 with chains A and B shown in electrostatic and ribbon representation, respectively. The surface gradient is colored with a red-to-blue gradient from −3 kBT/e to +3 kBT/e, highlighting polar interactions between SRs and EF1-2. (*F*) Surface representation of the *Eh*Actn2 dimer highlighting the twist in the rod domain. F-actin–binding site 1 (ABS1) is colored in orange. (*G*) Close-up view of *D* showing the insertion of EF1-2 within the rod domain. Polar interactions stabilizing the *Eh*Actn2 dimer are indicated.

(19). Accordingly, intracellular Ca^{2+} levels rapidly increase upon parasite adherence to target cells (20) and Ca^{2+} antagonists, channel blockers, and chelators significantly decrease the rate of phagocytosis in parasite trophozoites (20, 21). Many Ca^{2+}-sensitive ABPs have been reported to modulate actin dynamics and participate in *E. histolytica* phagocytosis. Among them are Ca^{2+}-binding proteins 1 and 3 (*Eh*CaBP1 and *Eh*CaBP3), coactosin, and α-actinin. While the role of the former three has been investigated in detail (21–23), little is known about α-actinin function and regulation in amoebic biology.

Here we report the crystal structures of Ca^{2+}-free and Ca^{2+}-bound α-actinin isoform 2 from *E. histolytica* (*Eh*Actn2), which is similar to the ancestral α-actinin. Structural analyses together with biophysical and biochemical studies provide the molecular basis for regulation by Ca^{2+}, in which Ca^{2+} binding to the CaMD controls F-actin–bundling activity by modulating *Eh*Actn2's multidomain flexibility. This mechanistic model paves the way to understanding regulation by Ca^{2+} in members of the spectrin superfamily from higher eukaryotes. In addition, we show that regulation of *Eh*Actn2 by Ca^{2+} is in line with the role of this protein during phagocytic cup formation and closure before scission in *E. histolytica* trophozoites, which might aid in development of drugs against amoebiasis.

Results and Discussion

***Eh*Actn2 Structure Reveals a Unique Multidomain Architecture.** The 3.1-Å crystal structure of full-length *Eh*Actn2 was determined by a combination of single-wavelength anomalous dispersion and molecular replacement using the high-resolution structures of the two main individual domains, ABD and the central rod domain (Fig. 1*C* and *SI Appendix*, Figs. S1 and S2 *A* and *B* and Tables S1 and S2). The *Eh*Actn2 dimer is formed by the juxtaposed protomers related by a crystallographic twofold axis in a tetragonal space group (Fig. 1*D*). Electrostatic surface potential shows complementarities between interacting surfaces, leading to productive electrostatic interactions between opposing protomers (Fig. 1*E*). Charge complementarity seems to be a general principle of α-actinin quaternary structure assembly and stability, as also observed in human α-actinin-2 (*h*Actn2) (4, 24).

The ABD, comprising two calponin homology (CH) domains, displays a closed conformation both alone and in the full-length protein (*SI Appendix*, Fig. S2 *A*, *Left*). The overall CH1–CH2 arrangement is very similar to that found in ABDs from plectin-1, α-actinin, and filamin (*SI Appendix*, Table S3). Most ABDs from higher organisms contain stretches of residues N-terminal to the domain, ranging from 20 to 40 in human α-actinins and filamins (*SI Appendix*, Fig. S2 *A*, *Right*) to ∼170 residues in plectin-1. By contrast, no additional sequence is present in the ABD from *Eh*Actn2 or yeast α-actinin, which might have implications for different mechanisms of regulation and cellular localization that are believed to be encoded at the N terminus of α-actinin ABDs from higher organisms (25, 26). The ABD is linked to rod SR1 by an 18-turn helix (the neck), thus forming a continuous 66-residue helix encompassing ABD C-terminal and SR1 N-terminal helices (Fig. 1*D*). The rod domain displays a torsional twist of ∼90° along the central axis, as also observed in *h*Actn2 (4, 24), which leads to an ∼90° rotation of ABDs and therefore F-actin–binding sites in the dimer (Fig. 1*F*) (27, 28). Assuming a rigid *Eh*Actn2 dimeric assembly, such an orientation of ABDs would impair bundling of parallel or antiparallel F-actins. Further *Eh*Actn2 crystal structures determined in a different space group revealed the presence of a hinge in the neck region (see below), thus explaining how the proper relative orientation of ABDs is achieved.

The position of EF1-2 represents the most striking difference between the structures of *h*Actn2 and *Eh*Actn2. In the former, EF1-2 leans on the rod (4), while in the latter, the EF1-2 h1 helix is sandwiched between SR1 and SR2 and stabilized by a mixture of electrostatic and hydrophobic interactions, mainly between the SR1 h2 and SR2 h3 helices (Fig. 1*G* and *SI Appendix*, Fig. S2*C* and Table S4). The rest of EF1-2 is solvent-accessible, including the Ca^{2+}-binding site (Fig. 1*G*). Comparison of dimerization interfaces from *Eh*Actn2 and the rod domain showed that the average solvation free energy gain upon dimerization was significant only in the former: $\Delta G = -24.6$ kcal/mol and P value 0.258 compared with $\Delta G = -1.5$ kcal/mol and P value 0.768 [$P > 0.5$ and $P < 0.5$ point to hydrophilic/unspecific and hydrophobic/specific interfaces, respectively (29)] (Fig. 1*D* and *SI Appendix*, Fig. S2*B*). This result indicates that the twisted SR1–SR2 antiparallel assembly in *Eh*Actn2 is energetically favorable and provides stability to dimer formation by sandwiching EF1-2 in a specific conformation.

To assess the unique position of EF1-2 and the role of EF3-4 in assembly stabilization, we designed a series of internal cysteine residues based on the structure of the rod (*SI Appendix*, Fig. S2 *B* and *D*). Disulfide bonds were formed when cysteine residues were introduced into the *Eh*Actn2 rod alone, leading to formation of a covalently stable dimeric species (*SI Appendix*, Fig. S2*E*). By contrast, only monomers were observed under the same conditions when these mutations were introduced into full-length *Eh*Actn2 and ΔEF3-4 (*SI Appendix*, Figs. S1 and S2*E*), indicating that EF3-4 is not essential for correct intercalation of EF1-2 and confirming that EF1-2 is also positioned between SRs in solution.

Apart from having a pivotal role in dimer stabilization, EF1-2 is the only EF-hand motif in *Eh*Actn2 that binds Ca^{2+}, as predicted by Virel et al. (30, 31) and confirmed here by anomalous difference Fourier analysis using a low-energy dataset (*SI Appendix*, Table S2). Comparison of EF1-4 from our Ca^{2+}-bound *Eh*Actn2 structure with that from a Ca^{2+}-free NMR structure [Protein Data Bank (PDB) ID code 2M7L (30)] revealed that the two lobes display different relative orientations (rmsd value of 2.1 Å, *m* score 0.54) (*SI Appendix*, Fig. S3*A*) but similar overall structure (rmsd values of 2.2 Å [*m* score 0.90] and 1.9 Å [*m* score 0.82] for EF1-2 and EF3-4, respectively) (*SI Appendix*, Fig. S3*B*). The *m* score reflects the proportion of superposable residues between two structures (for an *m*-score definition, see *SI Appendix*, *Materials and Methods* and ref. 32). The extent of structural changes leading to closed-to-open transitions in EF-hand motifs varies among Ca^{2+}-binding proteins. To quantitatively compare the conformational differences, we calculated and compared θ and φ angles between entering and exiting helices. While EF1-2 displays the same semiopen conformation both in the crystal and in solution, EF3-4 exhibits a semiopen conformation in the former and a closed one in the latter, as helix h1 is moved away to accommodate the neck (Fig. 1*D* and *SI Appendix*, Table S5). A similar semiopen conformation is observed in the CaMD of *h*Actn2 in which EF3-4 similarly binds to the neck (or titin *Z* repeats) and in calmodulin bound to myosin calmodulin binding motifs (IQ) (4, 33–35), as dictated by the hydrophobic network with the respective interacting partner (see below and ref. 33). Comparison of individual EF-hand motifs in the *Eh*Actn2 structure showed an rmsd value of 2.4 Å (*m* score 0.82). The major difference between EF1-2 and EF3-4 is found at helix h1 (*SI Appendix*, Fig. S3*C*), which in the former is locked between the SRs of the dimer and in the latter is bound to the neck (Fig. 1 *D* and *G* and *SI Appendix*, Fig. S2*C*) (4), thus providing each EF-hand motif with a different functionality.

In summary, full-length *Eh*Actn2 is an antiparallel dimer with an internal twist that results in a perpendicular orientation of ABDs, as also observed in *h*Actn2. The major difference between the ancestral and modern α-actinins is the position of EF1-2, which in the former is firmly sandwiched between the two subunits and contributes to the stability of the dimer.

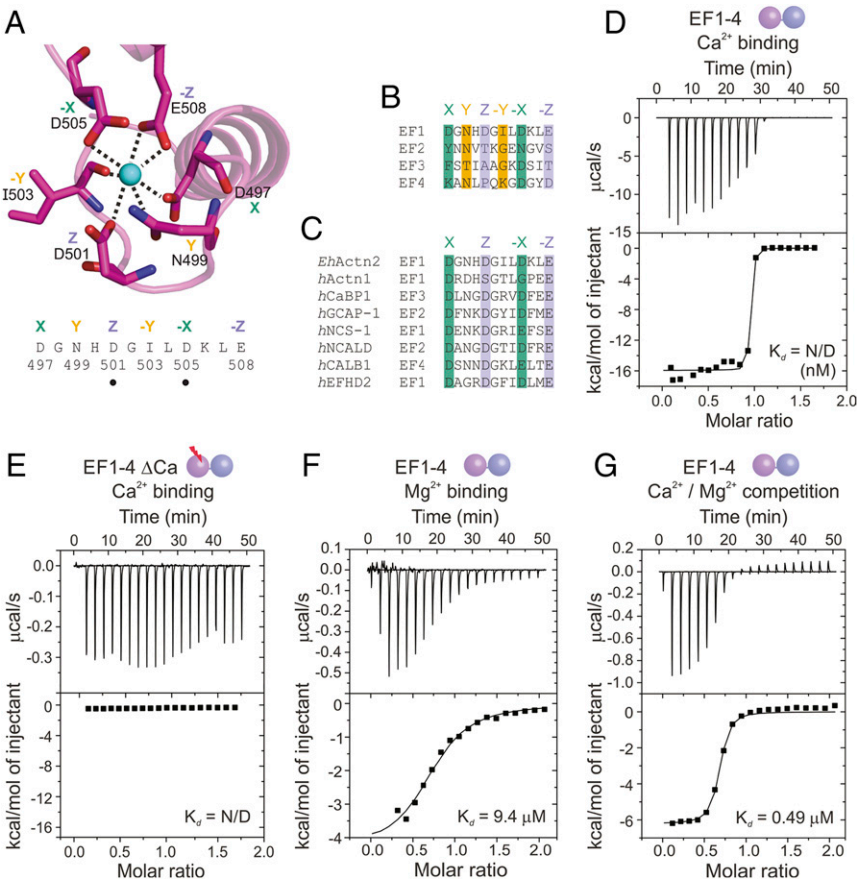

Fig. 2. *Eh*Actn2 shows exceptionally high affinity for Ca^{2+} and is regulated by Ca^{2+} in the presence of Mg^{2+}. (*A*) Structure of the Ca^{2+}-binding loop of *Eh*Actn2 EF1-2 shown in a ribbon representation. Residues involved in the Ca^{2+}-binding coordination sphere are shown in green (*X*, −*X* axes), orange (*Y*, −*Y* axes), and violet (*Z*, −*Z* axes). Positions of generated mutants are indicated with a dot. (*B*) Sequence alignment of potential Ca^{2+}-binding loops in *Eh*Actn2 EF hands. Same color code as in *A*. (*C*) Sequence alignment of Ca^{2+}-binding loops for *Eh*Actn2 EF1 and other calcium-binding proteins with nanomolar Ca^{2+} affinity. *h*Actn1, human α-actinin-1 (UniProt [UP] code P12814); *h*CaBP1, human calcium-binding protein 1 (UP code Q9NZU7); *h*GCAP-1, human guanylyl cyclase-activating protein 1 (UP code P43080); *h*NCS-1, human neuronal calcium sensor 1 (UP code P62166); *h*NCALD, human neurocalcin-delta (UP code P61601); *h*CALB1, human calbindin (UP code P05937); *h*EFHD2, human EF-hand domain-containing protein D2 (UP code Q96C19). Color-coded as in *A*. (*D*–*G*) ITC profiles of Ca^{2+} binding to EF1-4 (*D*); Ca^{2+} binding to EF1-4 ΔCa (*E*); Mg^{2+} binding to EF1-4 (*F*); and Ca^{2+} binding to EF1-4 in the presence of Mg^{2+} (*G*). Determined K_d values are indicated. N/D, not determined.

***Eh*Actn2 Shows Exceptionally High Affinity for Ca^{2+} and Is Regulated by Ca^{2+} in the Presence of Mg^{2+}.** In EF1-2 *Eh*Actn2, Ca^{2+} is coordinated by seven protein atoms arranged in a distorted pentagonal bipyramid configuration. The six residues involved in Ca^{2+} binding are D497, N499, D501, I503, D505, and E508 at distances ranging from 2.2 to 2.8 Å, except D505, which is farther away (3.2 Å) (Figs. 1*D* and 2*A*). This latter residue is typically bridged to Ca^{2+} by a water molecule, which we could not locate in our 3.1-Å electron density map. Sequence alignments revealed that only EF1 can bind Ca^{2+} (Fig. 2 *B* and *C*), in agreement with previous predictions (30), our intact mass spectrometry analysis on *Eh*Actn2 and EF1-4, and binding assays using a high Ca^{2+}-affinity fluorescent dye (*SI Appendix*, Fig. S4 *A* and *B*).

To characterize Ca^{2+}–*Eh*Actn2 interaction and its impact on protein regulation, we first investigated the Ca^{2+}-binding affinity of EF1-2 and EF1-4 alone as well as EF hands in the context of the full-length protein. Our isothermal titration calorimetry (ITC) experiments showed a very high affinity of EF1-2 and EF1-4 for Ca^{2+}, with a K_d in the low-nanomolar range and a binding stoichiometry close to 1 (Fig. 2*D* and *SI Appendix*, Fig. S4*C*). By contrast, EF1-4 ΔCa, with three point mutations in the EF1 loop (*SI Appendix*, Table S1), did not bind Ca^{2+} (Fig. 2*E*). Comparison of the coordination spheres of *Eh*Actn2 EF1-2 with those of other CaMDs displaying high Ca^{2+} affinity revealed a privileged residue arrangement in their binding loop (Fig. 2*C*). These EF-hand motifs follow the so-called acid-pair hypothesis in which high affinity is driven by acidic residues involved in Ca^{2+} coordination positioned opposite each other on the *X*, *Y*, or *Z* axis (36), namely D497/D505 and D501/E508 for the *X* and *Z* axes, respectively, in *Eh*Actn2 EF1-2 (Fig. 2 *A* and *C*). To confirm the privileged *Eh*Actn2 Ca^{2+} coordination architecture, we generated the D501N and D505N mutants that exhibited much weaker K_d values (0.20 and 0.28 µM, respectively) than the wild type (WT) EF1-4 (*SI Appendix*, Fig. S4 *D*–*F* and Table S6). Accordingly, the human α-actinin-1 CaMD, which does not display an acid-pair coordination sphere (Fig. 2*C*), binds Ca^{2+} with lower affinity (K_d of 50 to 100 µM) (37, 38). Although it was not possible to obtain binding isotherms for full-length *Eh*Actn2, we confirmed that its Ca^{2+} affinity was comparable to that of EF1-2 and EF1-4 by using a competition assay with a low Ca^{2+}-affinity fluorescent dye (*SI Appendix*, Fig. S4 *G* and *H*). Our determined affinity differs notably from that previously reported, where Ca^{2+} binding of *Eh*Actn2 was found to be weaker than that of calmodulin (30, 31). This result might be explained by different sample purification protocols, which could lead to partially Ca^{2+}-loaded samples in previous experiments, and by the different buffer conditions and methods used.

The exceptionally high affinity of *Eh*Actn2 EF1-2 for Ca^{2+} correlates with that of proteins acting as Ca^{2+} buffers rather than Ca^{2+} sensors (39), and therefore poses the question as to whether *Eh*Actn2 function can be regulated in vivo. EF hands can bind both Ca^{2+} and Mg^{2+}, and the concentration of Mg^{2+} in resting eukaryotic cells is around 0.1 to 1.0 mM (40), thus exceeding Ca^{2+} concentration by ∼1,000-fold. We therefore anticipated that the presence of Mg^{2+} would significantly decrease *Eh*Actn2 Ca^{2+} affinity. To test this, we first determined the affinity of EF1-4 for Mg^{2+}, revealing a K_d of 9.39 µM (Fig. 2*F* and *SI Appendix*, Table S6), and next performed a competition Ca^{2+} titration assay in the presence of 1 mM Mg^{2+} (Fig. 2*G* and *SI Appendix*, Table S6). Under these conditions, EF1-4 Ca^{2+} affinity decreased to 0.49 µM. A competition assay further allowed us to estimate the K_d of *Eh*Actn2 EF1-2 for Ca^{2+} to be 5.30 nM (*SI Appendix*, Table S6).

We conclude that *Eh*Actn2 can indeed be regulated by Ca^{2+} under physiological conditions.

Ca^{2+} and Mg^{2+} Binding Stabilizes *Eh*Actn2 Structure. To elucidate the effect of Ca^{2+} on *Eh*Actn2 function, we determined the crystal structures of a Ca^{2+}-free (Ca^{2+}-insensitive mutant, hereafter ΔCa; *SI Appendix*, Table S1) and of an additional Ca^{2+}-bound form, both of which crystallized in the same orthorhombic space group, thus enabling a direct comparative structural analysis. Structures were refined to a similar resolution, 3.3 Å for the former and 3.1 Å for the latter (Fig. 3*A* and *SI Appendix*, Table S2). As for Ca^{2+}-bound tetragonal *Eh*Actn2, in both orthorhombic structures the functional dimer is formed by a crystallographic twofold axis. EF1-2 also remains locked between SR1 and SR2 in both orthorhombic structures, which show overall moderate conformational changes in EF1-4, with rmsd values of ∼1.0 and ∼0.9 Å (both *m* score 0.95) between orthorhombic Ca^{2+}-bound and ΔCa structures and the two Ca^{2+}-bound structures, respectively. The central rod domain is very similar in all three structures, with individual SRs and the tandem SR1–SR2 superimposing with rmsd values in the range of ∼0.5 Å (*m* score 0.99). In the ΔCa structure, the Ca^{2+}-binding loop displays a different conformation and a higher thermal mobility due to the absence of Ca^{2+}, which has a structuring effect (Fig. 3 *A* and *B*). The difference in angle between incoming and exiting helices upon Ca^{2+} binding increases only from 113° in the Ca^{2+}-free protein to 116° in the Ca^{2+}-bound orthorhombic form (*SI Appendix*, Fig. S3*D* and Table S5). This is common in proteins that act as Ca^{2+} buffers, while larger changes in interhelical angles are common in proteins that act as Ca^{2+} sensors (41).

ABDs conserve the closed conformation but adopt different orientations in each structure: In the Ca^{2+}-bound orthorhombic structure, we observed a rotation of 135° along the rod axis compared with that in the Ca^{2+}-bound tetragonal one, and of an additional 86° in the ΔCa orthorhombic structure (Fig. 3*A* and *SI Appendix*, Fig. S3*F*). ABD orientational flexibility was also observed in *h*Actn2, which highlights the built-in flexibility of the neck region as a conserved property within the α-actinin family (4, 42). In both orthorhombic structures, the ABD forms different polar contacts with the CaMD, denoting the transient nature of the interaction. In addition, the ABD is engaged in crystal contacts with symmetry-related molecules, indicating that one of many possible orientations is stabilized in the crystal lattice. Furthermore, and unlike in *h*Actn2, in the tetragonal crystal form there are no contacts between EF3-4 and ABD, which points to the EF3-4–neck interaction as the key regulator for ABD positioning in *Eh*Actn2 (see below).

As structural analyses did not reveal large conformational differences between Ca^{2+}-free and Ca^{2+}-bound CaMD structures, we next looked for indicators of differential structural mobility. We found a notably increased thermal mobility in the ΔCa form, especially for the ABD, the neck region preceding the EF3-4–binding site, and EF3-4 helices h2, h3, and h4 along with their connecting loops (Fig. 3 *A*, *Bottom*). Consistently, the ΔCa structure displays weaker electron density and several poorly resolved connecting loops in the ABD and CaMD. The increased ABD orientational flexibility is rooted at the hinge of the neck region that links the ABD and rod, and decreases upon Ca^{2+} binding. This agrees with a decreased hinge length, which spans residues 223 to 241 and 229 to 233 in the ΔCa and Ca^{2+}-bound orthorhombic structures, respectively (Fig. 3 *A* and *B* and *SI Appendix*, Fig. S3*F*). This hinge functionally resembles those found in *h*Actn2, which are located at the beginning and end of the neck region (*SI Appendix*, Fig. S3*F*) (4), allowing proper relative orientation of the ABDs with respect to the rigid twisted rod and therefore proper F-actin–bundling activity.

To support our findings on increased structural mobility of the Ca^{2+}-free form, we measured the melting temperatures (T_ms) of *Eh*Actn2 upon Ca^{2+} and Mg^{2+} binding. Differential scanning fluorimetry (DSF) revealed T_m values of 57.1 and 60.1 °C for *Eh*Actn2 in the absence and presence of Ca^{2+}, respectively, while those for ΔCa were similar in both conditions (57.2 and 56.0 °C) (*SI Appendix*, Fig. S5*A*). Mg^{2+} had an intermediate effect on *Eh*Actn2 thermal stability, yielding a T_m of 58.3 °C. Limited proteolysis experiments further corroborated these results, as ΔCa was digested more efficiently than *Eh*Actn2 in Ca^{2+}, and Mg^{2+}-bound *Eh*Actn2 was more resistant to proteolysis than ΔCa (*SI Appendix*, Fig. S5*B*). In addition, Ca^{2+} binding promoted an increase in secondary structure content of both EF1-2 and EF1-4, as shown by circular dichroism (CD) molar ellipticity at 200, 208, and 222 nm (*SI Appendix*, Fig. S5*C*). Finally, we assessed Ca^{2+}-bound *Eh*Actn2 and ΔCa structural flexibility in solution using size-exclusion chromatography coupled to multiangle light scattering (SEC-MALS), small-angle X-ray scattering (SAXS), and time-resolved fluorescence anisotropy (FA) (*SI Appendix*, Fig. S6). However, we could not find significant differences in derived molecular parameters between the two forms, which means that changes are subtle and cannot be detected due to resolution limits of the techniques. This is supported by the good fit (χ of ∼1.5) between crystal structures and SAXS data in both cases (*SI Appendix*, Fig. S6).

Altogether, our data show that binding of both Ca^{2+} and Mg^{2+} stabilizes *Eh*Actn2 structure, with Ca^{2+} having a greater effect, even though this effect does not result in major structural changes.

Interactions between EF3-4 and the Neck Govern *Eh*Actn2 ABD Orientational Flexibility. To understand the structural determinants of ABD orientational flexibility, we analyzed the interactions between EF3-4 and the neck region. EF3-4 wraps around the neck of the juxtaposed protomer in a 1:1 or canonical interaction (43), which involves the hydrophobic cleft between the two EF hands (∼19% of total surface area) and the canonical hydrophobic Ca^{2+}/calmodulin-binding motif of the neck (Fig. 3*C*). This motif is termed 1-4-5-8 and in the case of *Eh*Actn2 comprises residues G238, A241, G242, and L245 (44). An additional buried phenylalanine (F244) and two hydrogen bonds found between EF3-4 and SR1 further stabilize the position of the CaMD lobe (Fig. 3*C* and *SI Appendix*, Table S4).

Comparison of the relative domain arrangement between the Ca^{2+}-bound and ΔCa structures showed loosened interactions between EF3-4 loop h2–h3 plus the h3 helix and the neck region for ΔCa, as inferred from the interface analysis of the EF hands and the rest of the dimer, revealing an increased distance between the centers of mass of EF3-4 and the neck (12.6 Å for Ca^{2+}-bound and 13.5 Å for ΔCa) (Fig. 3*B*). While all three structures display a similar number of electrostatic interactions, the average solvation free energy gain is very similar for the two Ca^{2+}-bound forms (about −21 kcal/mol) and significantly lower for the ΔCa structure (−13.4 kcal/mol) (*SI Appendix*, Tables S7 and S8). Inspection of solvation energy contributions from individual residues showed that EF1-2 displays a similar pattern in all three structures as this motif is firmly sandwiched between SR1 and SR2 via the EF1 h1 helix. Substantial differences appear, however, in the neck region, in EF3-4 h1 and h3 helices, and in the h2–h3 connecting loop, all of which display increased thermal mobility (Fig. 3*B*). Specific residues in both Ca^{2+}-bound structures contribute similarly to the EF3-4–neck interacting interface by providing high solvation energy while the contribution is significantly lower for the ΔCa structure (Fig. 3*D*), in agreement with movement of the neck by about 1.5 Å toward the h1–h2 groove upon Ca^{2+} binding and increase of the interaction interface area (*SI Appendix*, Fig. S3*E* and Table S7).

Our structural analysis reveals that Ca^{2+} binding strengthens the EF3-4–neck interaction, causing reduced flexibility at the hinge of the neck region preceding the CaMD-binding site (Fig. 3 *A* and *B* and *SI Appendix*, Fig. S3*F*), which in turn reduces ABD orientational flexibility. To further validate this, we designed three different constructs, namely NEECK, NEECK#, and ΔEF3-

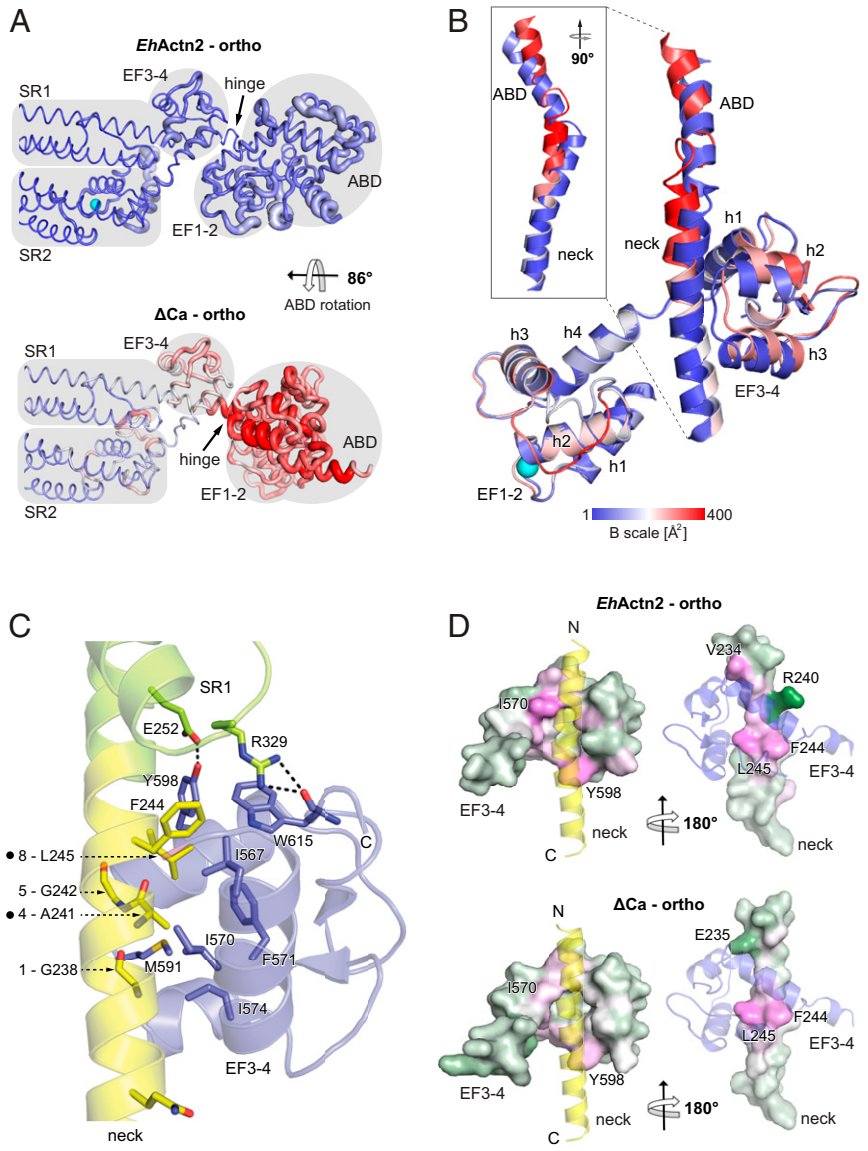

Fig. 3. Ca^{2+} binding stabilizes the *Eh*Actn2 structure. (*A*) B-factor representation of Ca^{2+}-bound and Ca^{2+}-free (ΔCa) *Eh*Actn2 structures crystallized in the same orthorhombic space group. The color code from blue to red shows the absolute B factors, coil thickness represents the relative difference in B factors, and domain boundaries are shaded in gray. (*B*) Superposition of EF1-2 from Ca^{2+}-bound *Eh*Actn2 and ΔCa showing the conformational differences in the neck and EF3-4 (plus a part of the ABD C-terminal α-helix). The structures are colored according to absolute B factors as in *A*. (*C*) Ribbon representation of the major polar and hydrophobic interactions between the neck region (yellow) and EF3-4 (blue). Positions of generated mutants are indicated with a dot next to the neck 1-4-5-8 motif. (*D*) Surface representation of the neck and EF3-4 from Ca^{2+}-bound *Eh*Actn2 and ΔCa colored based on residue solvation energy contributions (green corresponds to negative contribution, white to neutral, and magenta to positive). A positive value makes a negative contribution to the solvation energy gain of the interface, corresponding to a hydrophobic effect. Two orientations rotated by 180° are shown, in which the interacting domain is represented as a transparent ribbon.

4. The former two contained, respectively, two and one point mutations in the neck 1-4-5-8 motif designed to abrogate the hydrophobic EF3-4–neck interaction, while the latter lacked EF3-4 (Fig. 3*C* and *SI Appendix*, Fig. S1 and Table S1). In SEC-MALS, both NEECK and NEECK$^{\#}$ eluted at decreased volumes compared with *Eh*Actn2 (*SI Appendix*, Fig. S6 *A* and *B*), indicating a larger hydrodynamic volume of the particle. SAXS data revealed that NEECK and ΔEF3-4 displayed smaller R_g and D_{max} values than *Eh*Actn2 (6.4 and 24.5 nm, and 6.2 and 23.0 nm vs. 6.8 and 27.0 nm) (*SI Appendix*, Fig. S6 *C* and *D*), which together with Kratky plots indicate a deviation from the typical α-actinin rod-like shape due to abrogation of the EF3-4–neck interaction and consequent increased ABD orientational flexibility (*SI Appendix*, Fig. S6 *E* and *F*). This result was supported by time-resolved FA experiments in which *Eh*Actn2 and NEECK were labeled at the N terminus of the ABD. The former displayed ∼2.5 times higher FA and rotational lifetime values than NEECK (*SI Appendix*, Fig. S6 *G–I*), in agreement with a more compact and less dynamic particle.

We conclude that the EF3-4–neck interaction governs ABD orientational flexibility via stabilization/destabilization of the hinge in the neck region.

Ca^{2+} Binding to EF1-2 Regulates *Eh*Actn2 In Vitro F-Actin–Bundling Activity by Modulating ABD Flexibility. To assess whether Ca^{2+}-regulated ABD flexibility translates into *Eh*Actn2 function, we investigated F-actin–bundling activity using low-speed cosedimentation assays. The presence of Ca^{2+} compromised *Eh*Actn2 bundling, particularly at low molar ratios of *Eh*Actn2:F-actin that are likely to reflect more physiological conditions (Fig. 4*A* and *SI Appendix*, Figs. S7*A* and S8 *A* and *B*). This finding agrees with previous experiments (31) and was further corroborated here by electron microscopy (EM) of negatively stained specimens, in which the presence of Ca^{2+} completely inhibited the formation of F-actin bundles. The same result was obtained when 1.5 mM Mg^{2+} was added to 1.5 μM Ca^{2+} (*SI Appendix*, Fig. S8*C*), mimicking conditions in which *Eh*Actn2 can be Ca^{2+}-regulated in vivo. As expected, the bundling ability of ΔCa, which is unable to bind Ca^{2+}, was Ca^{2+}-independent (Fig. 4*B* and *SI Appendix*, Figs. S7*B* and S8*B*). In addition, the bundling activity of *Eh*Actn2 was not inhibited by Mg^{2+} (*SI Appendix*, Fig. S8*D*), thus confirming that *Eh*Actn2 is a truly Ca^{2+}-regulated protein even though it is able to bind Mg^{2+}. NEECK and ΔEF3-4, exhibiting a highly flexible ABD, completely failed to bundle F-actin both in the absence and presence of Ca^{2+} (Fig. 4 *C* and *D*

and *SI Appendix*, Figs. S7 *C* and *D* and S8*B*). These results were validated by EM of negatively stained specimens, which showed that ΔCa is able to bundle F-actin to a similar extent in the absence and presence of Ca^{2+}, whereas NEECK and ΔEF3-4 are unable to bundle F-actin under any tested condition. NEECK$^{\#}$, containing a single mutation in the neck, also failed to bundle F-actin (*SI Appendix*, Fig. S8*E*). Together, these results demonstrate that the EF3-4–neck interaction is key to restraining proper ABD orientational sampling and further support our view of a highly precise and sensitive regulatory mechanism for this protein.

To determine *Eh*Actn2 F-actin–binding capacity, we used high-speed cosedimentation assays. Both *Eh*Actn2 and ΔCa showed a similar apparent K_d in the absence and presence of Ca^{2+} (*SI Appendix*, Fig. S8 *G* and *H*). However, B_{max} values for Ca^{2+}-free *Eh*Actn2 and ΔCa were 2 to 2.5 times higher than that of Ca^{2+}-bound *Eh*Actn2, implying a lower number of *Eh*Actn2 molecules bound to F-actin, which correlates with an inhibitory effect of Ca^{2+} on F-actin bundling. We ascribe the increase of B_{max} values to an increased flexibility of the neck region in the absence of Ca^{2+}, leading to increased protein mobility that is likely to result in sterical hindering of adjacent α-actinin–binding sites on F-actin. F-actin–binding affinity of NEECK and ΔEF3-4 was notably increased, as inferred from significantly lower apparent K_d values compared with those of *Eh*Actn2 regardless of the presence of Ca^{2+} (*SI Appendix*, Fig. S8 *I* and *J*). However, NEECK and ΔEF3-4 exhibited significantly lower B_{max} values, that is, a lower total number of molecules bound to F-actin. Both increased affinity and decreased stoichiometry are consistent with a highly flexible ABD that facilitates association with F-actin, but precludes the binding of adjacent *Eh*Actn2 molecules.

Proteins that cross-link F-actin can form either bundles of (anti)parallel filaments or isotropic networks, both of which have very different viscoelastic properties (45–47). F-actin bundles behave as a viscous fluid, whereas F-actin isotropic networks behave as a solid. The effect of a protein cross-linker on the viscoelastic properties of F-actin networks can be assessed by rheology by measuring the magnitude of the complex modulus and phase shift of mixtures of F-actin with cross-linker (46, 48). The magnitude of the complex modulus (G^*) of a material measures its resistance to an oscillatory deformation as a function of the amplitude of deformation, while the phase shift (δ; delta) between the deformation and the response depends on whether the material is solid (0 radians) or fluid (1.6 radians). To address the effect of *Eh*Actn2 on F-actin gelation, we measured the rheological properties of F-actin in the presence of Ca^{2+} and a fixed concentration of different *Eh*Actn2 constructs. ΔEF3-4, exhibiting a highly flexible ABD, formed F-actin networks with similar resistance to that of F-actin alone (Fig. 4 *I* and *J*), which is in agreement with low-speed cosedimentation assays showing that ΔEF3-4 cannot bundle F-actin (see above and Fig. 4*D*). By contrast, ΔCa, mimicking Ca^{2+}-free *Eh*Actn2, formed F-actin networks more resistant to deformations and more solid-like at higher frequencies when compared with Ca^{2+}-bound *Eh*Actn2 (Fig. 4 *I* and *J*), indicating that the increased ABD flexibility in ΔCa results in "tight" solid-like F-actin networks, rather than in the formation of F-actin bundles only.

To further corroborate this, we measured the rheological properties of F-actin in the presence of Ca^{2+} and increasing concentrations of *Eh*Actn2 and ΔCa (Fig. 4 *K* and *L*). We could not see the formation of isotropic networks, most likely due to the low affinity of *Eh*Actn2 for F-actin (K_d of 4.19 μM; *SI Appendix*, Fig. S8*G*), as also previously observed for *Acanthamoeba* α-actinin (47). However, ΔCa started to bundle F-actin at lower F-actin:α-actinin molar ratios (15:1) than *Eh*Actn2 (Fig. 4 *K* and *L*, orange box), as inferred by increased resistance to deformation of the F-actin network with a concomitant increase in phase shift (see *SI Appendix*, *Materials and Methods* for interpretation of rheology data), indicating a more fluid-like behavior. This is in agreement with bundling assays carried out at similar F-actin:α-actinin molar ratios (i.e., 16:1; Fig. 4 *A* and *B*, orange box). At higher concentrations, *Eh*Actn2 formed bundles while ΔCa formed F-actin networks with increased resistance to deformation and concomitant decrease in phase shift, indicating the formation of tight solid-like F-actin networks that are most likely the result of unregulated bundling caused by increased ABD flexibility.

Taken together, our results show that binding of Ca^{2+} inhibits *Eh*Actn2 F-actin–bundling activity without significantly affecting F-actin–binding affinity, thus modulating the nature of the F-actin network required for a specific cellular function.

Ca^{2+}-Induced Interdomain Cross-Talk Regulates *Eh*Actn2 In Vitro F-Actin–Bundling Activity via Multidomain Flexibility. To this point, the presented data show that 1) the key EF3-4–neck interaction determines ABD orientational flexibility; 2) a hinge at the N terminus of the neck region allows ABD rotation around the rod axis; and 3) Ca^{2+} binding to *Eh*Actn2 EF1-2 triggers increased structural rigidity resulting in decreased ABD motional properties. But how is the effect of Ca^{2+} binding transmitted from EF1-2 to ABD in the absence of direct contacts between these two domains?

To gain further insights into interdomain cross-talk, we explored whether it is possible to rescue the function of ΔEF3-4 by reintroducing EF3-4 in the bundling assay. The presence of a 20-fold molar excess of EF3-4 did not affect the bundling capacity of ΔEF3-4 in the presence or absence of Ca^{2+} (Fig. 4*E*), indicating that the EF3-4–neck interaction relies on CaMD integrity. We therefore tried to restore the function of ΔEF1-4, which had likewise proved to be completely inert for F-actin bundling, by reintroducing EF1-4 or EF3-4 in the bundling experiment. We were able to nearly restore the activity of this variant when reintroducing the whole CaMD, but not with EF3-4 (Fig. 4 *F* and *G*). Thus, in the presence of EF1-4, ΔEF1-4 behaved similar to *Eh*Actn2, namely it was able to bundle F-actin without Ca^{2+} and its activity was reduced in Ca^{2+} (Fig. 4*G*). This result was confirmed by EM of negatively stained samples, in which the presence of bundles could only be detected when F-actin, ΔEF1-4, and EF1-4 were mixed together (Fig. 4*H* and *SI Appendix*, Fig. S9). The high variability observed in this "rescue" experiment in the presence of Ca^{2+} can be attributed to the fact that the rod domain is likely to be closed in ΔEF1-4, thus precluding proper insertion of EF1-2 within the rod, which highlights the importance of EF1-2 in regulating protein function. Accordingly, ITC experiments between EF1-4 and the rod did not show any binding. We also assessed the affinity of EF1-4 and EF3-4 for the neck region in order to validate our rescue experiments. EF1-4 bound to the ABD–SR1 construct (*SI Appendix*, Fig. S1 and Table S1) with a K_d of 3.68 μM, whereas binding of EF3-4 to the same construct was about 10 times weaker (*SI Appendix*, Fig. S9 and Table S6), proving that the presence of EF1-2 substantially contributes to effective binding of the whole CaMD to the neck region. As expected, EF1-4 was not able to bind to the ABD–SR1–NEECK construct, supporting the specificity of the EF3-4–neck hydrophobic interaction (*SI Appendix*, Fig. S9 *C* and *F*).

To further validate our hypothesis that EF1-2 sandwiching within the rod is necessary for *Eh*Actn2 function, we designed a chimeric construct (hereafter chimActn2; *SI Appendix*, Fig. S1 and Table S1) in which the rod domain from *Eh*Actn2 was replaced with that from *h*Actn2 (4). Although chimActn2 bound Ca^{2+} with the same affinity as *Eh*Actn2 when using a high Ca^{2+}-affinity fluorescent dye, its F-actin–bundling activity was not Ca^{2+}-sensitive (*SI Appendix*, Fig. S8*F*).

Together, our results demonstrate that the unique position of EF1-2 within the *Eh*Actn2 rod plays not only a structural but also a functional role, driving Ca^{2+} regulation by enabling interdomain cross-talk between the EF1 Ca^{2+}-binding site and the ABD via modulation of multidomain flexibility.

BIOCHEMISTRY

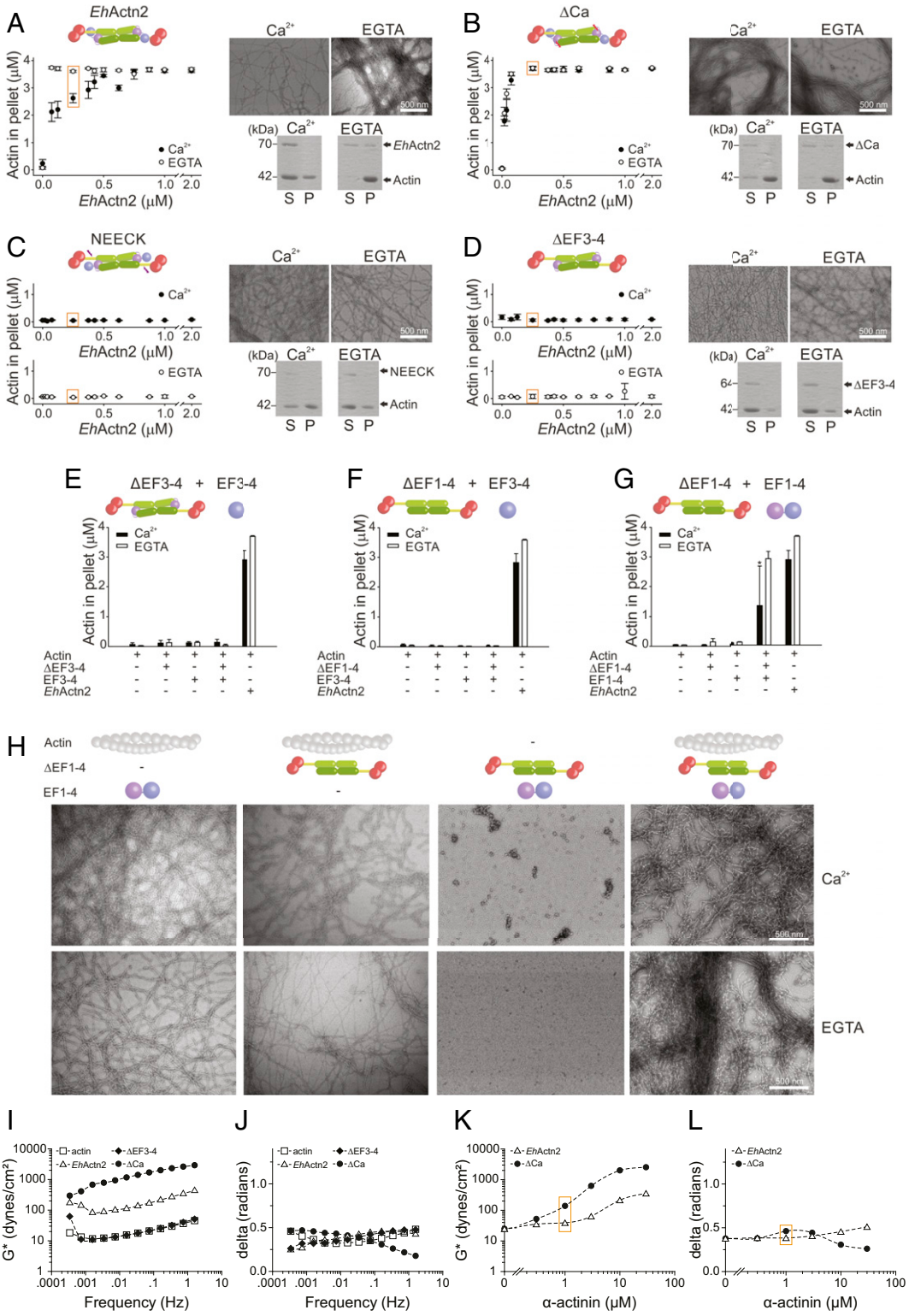

Fig. 4. Ca^{2+} binding regulates *Eh*Actn2 in vitro F-actin–bundling activity. (*A–D*) F-actin–bundling activity of *Eh*Actn2 constructs (*Eh*Actn2, ΔCa, NEECK, and ΔEF3-4; schematics are shown for clarity) measured at increasing protein concentrations of Ca^{2+} or ethylene glycol-bis(β-aminoethyl ether)-*N*,*N*,*N*′,*N*′-tetra-acetic acid (EGTA) (mean ± SD; same for *A–G*). Sodium dodecyl sulfate–polyacrylamide gel electrophoresis and EM analyses for negatively stained samples at 0.25 μM *Eh*Actn2 construct (S and P indicate supernatant and pellet fractions, respectively; scale bars are defined as indicated). (*E*) F-actin–bundling activity of ΔEF3-4 in the presence of a 20-fold molar excess of EF3-4 measured as in *A*. (*F*) F-actin–bundling activity of ΔEF1-4 in the presence of a 20-fold molar excess of EF3-4 measured as in *A*. (*G*) F-actin–bundling activity of ΔEF1-4 in the presence of a 20-fold molar excess of EF1-4 measured as in *A*. An asterisk indicates a significant difference, with $P = 0.033$ from Student *t* test. (*H*) EM of negatively stained F-actin–bundling "rescue" experiments of ΔEF1-4 plus EF1-4 measured as in *A*. (*I* and *J*) Rheology data showing magnitude (*I*) and phase shift (*J*) of the complex modulus for F-actin alone (15 μM) or mixed with *Eh*Actn2 constructs (10 μM). (*K* and *L*) Magnitude (*K*) and phase shift (*L*) of the complex modulus for F-actin alone (15 μM) or mixed with increasing concentrations of *Eh*Actn2 or ΔCa. Data were recorded at the same frequencies as in *I* and *K*, one of which (0.16 Hz) is shown. Data measured at similar F-actin:α-actinin molar ratios are boxed in orange.

EhActn2 Localizes to *E. histolytica* Cytoplasm and Plasma Membrane and Is Involved in Erythrophagocytosis. To assess the intracellular localization of *Eh*Actn2 in *E. histolytica* trophozoites, we carried out immunofluorescence imaging using a specific antibody raised against the *Eh*Actn2 rod and appropriate antibodies as markers for cytoplasm and cell membrane (*SI Appendix*, Fig. S10 *A* and *B*). *Eh*Actn2 localized to both cell membrane and cytoplasm in permeabilized cells, even though it was more abundant in cytoplasm, as revealed by quantitative analysis of images (*SI Appendix*, Fig. S10 *C–E*). However, in nonpermeabilized trophozoites, no staining was found at the inner leaflet of the membrane and suggesting *Eh*Actn2 association with cortical actin (*SI Appendix*, Fig. S10*F*). To validate *Eh*Actn2 subcellular localization, we carried out quantitative analysis of fluorescence using Pearson's correlation coefficient (PCC), which showed a higher degree of cytoplasmic ($r = 0.665$) vs. plasma membrane colocalization ($r = 0.479$) (*SI Appendix*, Fig. S10*G*). Together, our results indicate that *Eh*Actn2 is likely to be a cytosolic protein that is recruited to the membrane under certain conditions, possibly when actin dynamics are required. The subcellular distribution of *Eh*Actn2 is similar to that reported for a putative protein from the spectrin family shown to bind Gal/GalNAc lectin (49), which provides a plausible model for the interaction between the membrane and actomyosin cytoskeleton in *E. histolytica*.

Cytoskeleton dynamics play an important role in *E. histolytica* pathogenesis, as rapid actin turnover is required during invasion and phagocytosis of intestinal and extraintestinal tissues. We therefore investigated the role of *Eh*Actn2 in phagocytosis of red blood cells (RBCs), also known as erythrophagocytosis. This is a useful assay to study both phagocytic mechanisms and virulence potential, as RBC-containing *E. histolytica* trophozoites have been detected in the fecal material of patients suffering from intestinal amoebiasis (50). We incubated *E. histolytica* trophozoites with human RBCs for different amounts of time and stained with *Eh*Actn2 antibody and tetramethylrhodamine-phalloidin (TRITC-phalloidin). We observed *Eh*Actn2 at different phagocytic structures, from cups to closure of cups until the process of scission, but not in mature phagosomes (*SI Appendix*, Fig. S11*A*). Some newly formed phagosomes close to the plasma membrane (hereafter "nascent phagosomes") were enriched in both *Eh*Actn2 and F-actin and appeared to be tethered to the membrane through a mesh of *Eh*Actn2 and F-actin (*SI Appendix*, Fig. S11*C*). Additional quantitative analysis of signal intensities across these structures showed an incomplete overlap of fluorescent images in some areas, indicating physical separation of *Eh*Actn2 and F-actin (*SI Appendix*, Fig. S11*D*). A similar observation was reported for *Acanthamoeba* α-spectrin, which was found in nascent phagosomes near the membrane, but not in mature phagosomes (51). Further quantitative analysis of fluorescence using PCC showed a high degree of colocalization between *Eh*Actn2 and F-actin during phagocytic cup formation ($r = 0.906$) and closure of cups just before scission ($r = 0.819$) and in nascent phagosomes ($r = 0.675$) but not after complete separation of phagosomes from the membrane ($r = 0.265$), revealing that *Eh*Actn2 is present at the phagocytic cup during its formation and leaves during the process of scission (*SI Appendix*, Fig. S11 *B* and *E*).

These results together with our previous findings support *Eh*Actn2 colocalization with F-actin during phagocytic cup formation and scission.

Ca^{2+} Binding to *Eh*Actn2 Regulates *E. histolytica* Phagocytosis. To investigate the role of *Eh*Actn2 Ca^{2+} regulation in *E. histolytica* phagocytosis, we used different constructs, namely *Eh*Actn2-HA, ΔCa-HA, NEECK-HA, and ΔEF3-4-HA (*SI Appendix*, Table S1), all cloned into a constitutive vector requiring G418 (Geneticin) as selection agent. The C-terminal hemagglutinin (HA) tag did not alter in vitro F-actin–bundling activity nor *Eh*Actn2 cellular distribution in cells undergoing phagocytosis (*SI Appendix*, Fig. S12 *A* and *B*). In addition, *Eh*Actn2-HA showed high colocalization with endogenous *Eh*Actn2 and a similar degree of colocalization with F-actin at different phagocytic stages (*SI Appendix*, Fig. S12*C*). There was an increase in the level of *Eh*Actn2-HA (10%), ΔCa-HA (35%), NEECK-HA (20%), and ΔEF3-4-HA (30%) in cells grown using 30 μg/mL G418 compared with those grown using 10 μg/mL G418 (*SI Appendix*, Fig. S12*D*). By contrast, the amount of *Eh*Coactosin did not change in both G418 concentrations, proving that the effect was specific. All comparisons were made against cells carrying empty vector (i.e., without the gene of interest and HA tag) maintained at 30 μg/mL of G418. There was a marginal increase (6%) in phagocytosis in cells overexpressing *Eh*Actn2-HA after 30 min of incubation with RBCs (*SI Appendix*, Fig. S12*E*). However, RBC uptake was reduced by 45, 60, and 48% in cells overexpressing ΔCa-HA, NEECK-HA, and ΔEF3-4-HA, respectively.

Image inspection of ΔCa-HA–, NEECK-HA–, and ΔEF3-4-HA–overexpressing cells revealed the presence of many RBCs attached to the cells with no enrichment of HA-tagged protein at the interaction site (Fig. 5*A*), indicating that initiation of phagocytic cup formation was blocked. By contrast, phagocytic cups were visible in *Eh*Actn2-HA–overexpressing cells. Our interpretation of the visual analysis of the images was confirmed by a quantitative analysis (Fig. 5 *B* and *C*). These results demonstrate that the rates of both cup and phagosome formation are significantly reduced in cells overexpressing protein variants that cannot bind Ca^{2+} (ΔCa) or are impaired in F-actin–bundling activity due to abrogation of the EF3-4–neck interaction and concomitant increased ABD flexibility (NEECK and ΔEF3-4). Accordingly, the most pronounced defect was observed in NEECK-HA–expressing cells (Fig. 5 *B* and *C* and *SI Appendix*, Fig. S12*E*), in agreement with in vitro bundling and binding assays (Fig. 4*C* and *SI Appendix*, Fig. S8*I*). In addition, we quantified the fluorescence intensity of *Eh*Actn2-HA at the phagocytic cup and of ΔCa-HA, NEECK-HA, and ΔEF3-4-HA at the RBC attachment site. While there was an enrichment of the former, the latter was significantly reduced, indicating that these three protein variants are not recruited to phagocytic cups (*SI Appendix*, Fig. S13).

E. histolytica uses phagocytosis to obtain nutrients from the host, similar to other protists. Here we uncover that Ca^{2+} regulation of *Eh*Actn2–bundling activity contributes to this process. Any changes in *Eh*Actn2 that alter its Ca^{2+}-binding ability or F-actin–bundling capacity lead to defects in erythrophagocytosis. Given that there is no vaccine and only one effective drug class for treatment of amoebiasis (52), the design of compounds that specifically affect Ca^{2+} binding of *Eh*Actn2 might offer a new strategy to block host tissue destruction by *E. histolytica* trophozoites.

The Mechanistic Model of *Eh*Actn2 Provides Insights into Ca^{2+} Regulation of Human α-Actinins. The antiparallel dimeric architecture of both *Eh*Actn2 and *h*Actn2 dictates a perpendicular orientation of ABDs due to the twist embedded within the rigid rod domain, which inhibits their F-actin–bundling activity. Here we present a sensitive Ca^{2+} regulatory mechanism of an α-actinin similar to the ancestral α-actinin that is controlled by interdomain cross-talk and modulation of multidomain flexibility. Although EF1-2 Ca^{2+} binding does not cause significant conformational changes, it reduces protein dynamics by reinforcing the EF3-4–neck interaction and stabilizing the hinge region. This in turn reduces ABD orientational flexibility, leading to sterical inhibition of F-actin bundling (Fig. 6 *A* and *B*, *Top*). By contrast, dissociation of Ca^{2+} from α-actinin increases ABD orientational flexibility, which allows ABDs to adopt suitable and defined mutual orientations, enabling bundling of parallel or antiparallel F-actins (Fig. 6 *A* and *B*, *Bottom*). ABD flexibility

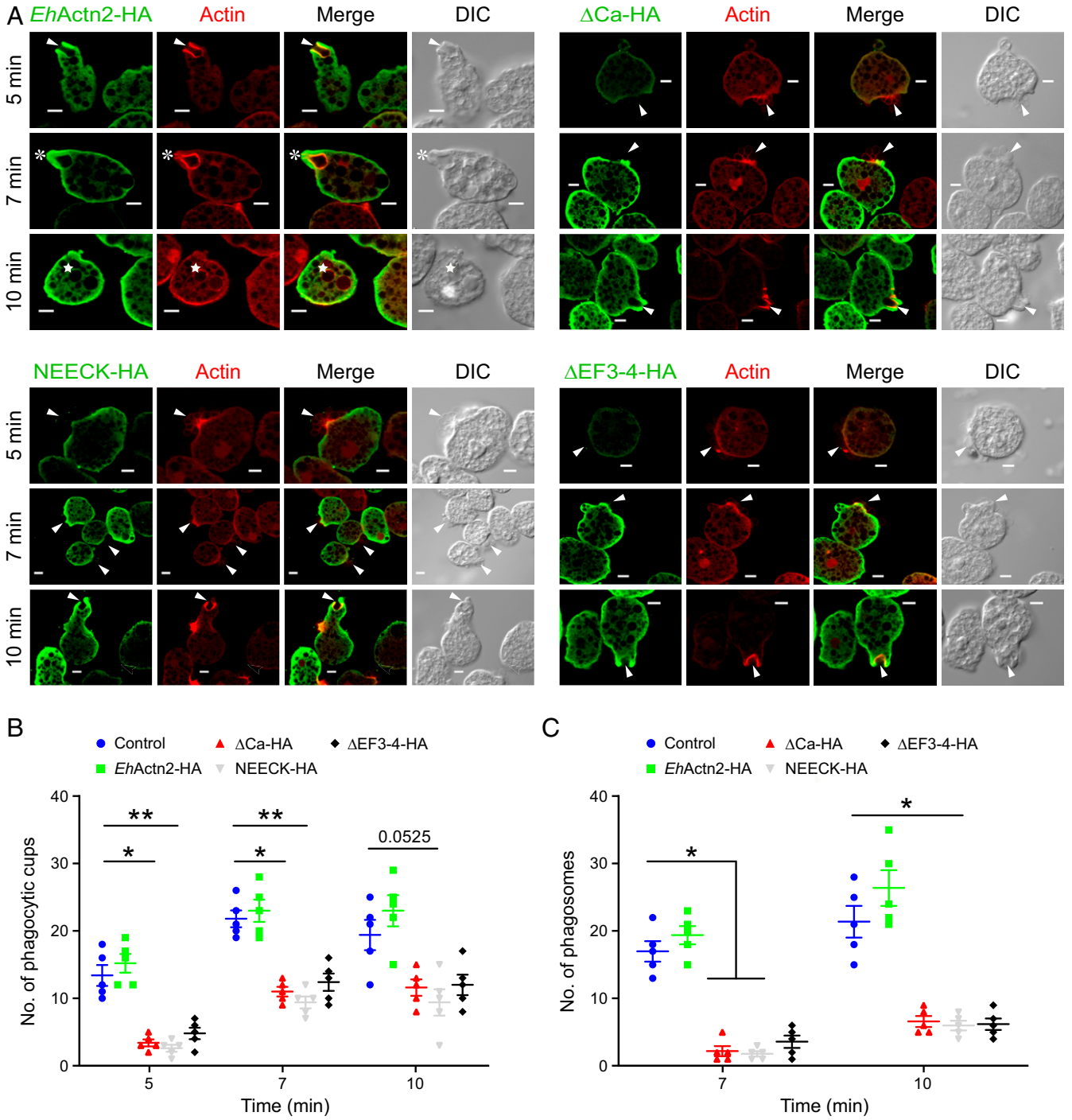

Fig. 5. Ca^{2+} binding to *Eh*Actn2 regulates *E. histolytica* phagocytosis. (*A*) Immunofluorescence imaging of overexpressed *Eh*Actn2 constructs (*Eh*Actn2-HA, ΔCa-HA, NEECK-HA, and ΔEF3-4-HA) and actin in *E. histolytica* trophozoites incubated with human RBCs for the selected time points. Arrowheads, asterisks, and stars indicate phagocytic cups, closed cups (just before scission), and phagosomes, respectively. (Scale bars, 5 μm.) (*B* and *C*) Quantitative analysis of phagocytic cups and phagosomes in trophozoites harboring an empty vector or overexpressing the same *Eh*Actn2-HA constructs as in *A*, carried out by randomly selecting 30 cells (in five sets) (mean ± SE). The number of cups and phagosomes increased after 7 min of incubation with RBCs by 6 and 12%, respectively, while at the same time point the number of cups and phagosomes decreased by 44 and 85%, 51 and 88%, and 41 and 79% in ΔCa-HA–, NEECK-HA–, and ΔEF3-4-HA–overexpressing cells, respectively. Kruskal–Wallis test followed by Dunn's multiple-comparison test was used for statistical comparisons (*$P \leq 0.05$, **$P \leq 0.005$), which were performed against the empty vector for each time point. HA denotes a C-terminal hemagglutinin tag.

is "encoded" in the hinge region of the neck, which seems to be a general feature in the α-actinin family, underscoring its importance in protein function (4, 42). Using classical biochemical terminology, we would describe Ca^{2+} as an allosteric regulator of F-actin–bundling activity by modulating ABD orientational flexibility. In addition, we uncover how the extent to which the EF3-4–neck interaction is stabilized is crucial for the fine-tuning of ABD flexibility and therefore regulation of *Eh*Actn2 function, as protein variants with "artificially" enhanced flexibility (i.e., NEECK, NEECK$^{\#}$, and ΔEF3-4) failed to bundle F-actin (Fig. 6 and *SI Appendix*, Fig. S14).

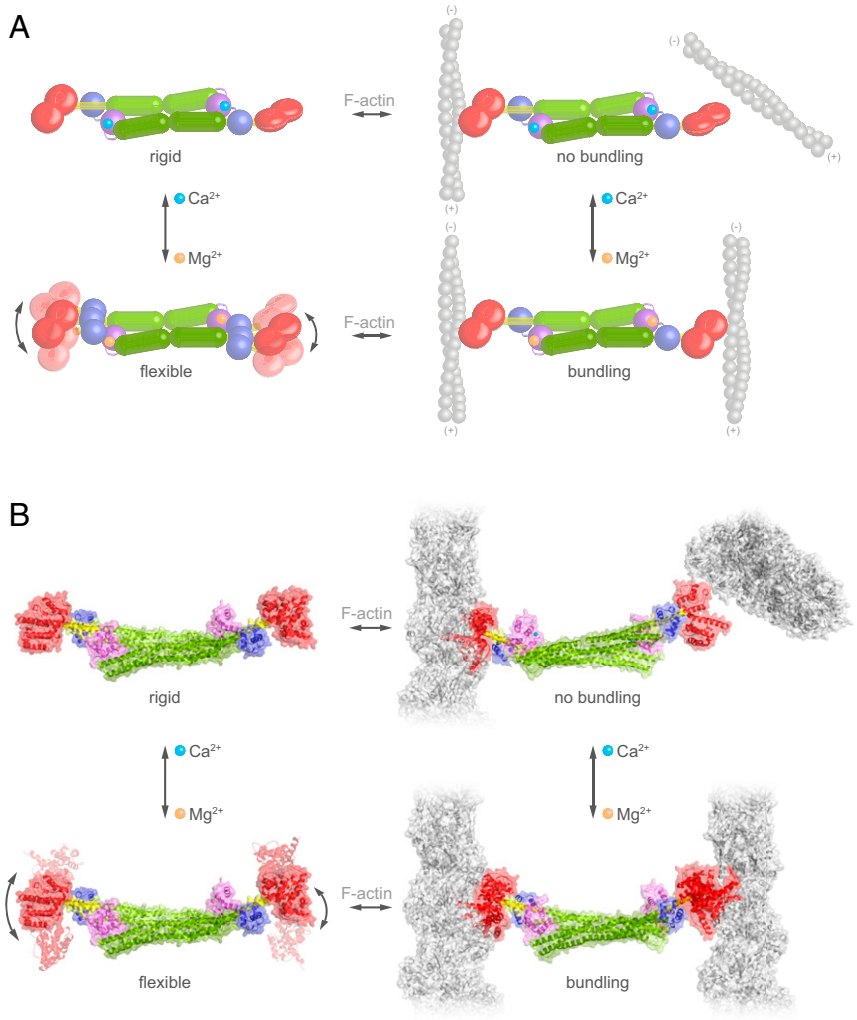

Fig. 6. Model for Ca^{2+} regulation of *Eh*Actn2 function. (*A*) Schematics illustrating the molecular changes in *Eh*Actn2 leading to reduced multidomain flexibility upon Ca^{2+} binding, which dictate F-actin–bundling activity. *Eh*Actn2 domains are shown as in Fig. 1. Ca^{2+} and Mg^{2+} ions are shown as cyan and orange spheres, respectively. (*B*) Same as in *A* including the structures of Ca^{2+}-bound and Ca^{2+}-free forms of *Eh*Actn2. Once the ABDs are flexibly attached to the rod domain, they could bundle parallel or antiparallel actin filaments. Here we chose a parallel orientation, which might be more representative for the phagocytic cup.

Even though the interaction of EF3-4 with the neck is canonical in both *Eh*Actn2 and *h*Actn2 (and with titin *Z* repeats) (4, 35), the two proteins are regulated differently, and respond to regulators in two fundamentally distinct ways at the molecular level. In *Eh*Actn2, EF3-4 remains bound to the neck in both Ca^{2+}-free and Ca^{2+}-bound states; however, Ca^{2+} binding causes stiffening of the neck region and reduced ABD orientational flexibility. In *h*Actn2, phosphatidylinositol bisphosphate (PIP_2) binding was reported to regulate the interaction with titin by releasing EF3-4(3-5). This results in an increase in ABD orientational flexibility and F-actin–bundling activity in one case and enables EF3-4 titin binding in the other. In contrast to *Eh*Actn2 NEECK, the equivalent open variant of *h*Actn2 can bundle F-actin (4), pointing to a more robust structure–function interplay in Ca^{2+}-insensitive α-actinins compared with Ca^{2+}-regulated forms.

The importance of proper ABD orientational flexibility for *Eh*Actn2 function is further highlighted by our in vitro and in vivo results. This might be a general mechanism for Ca^{2+}-regulated human α-actinin isoforms. Nevertheless, in these proteins, the detailed molecular translation of Ca^{2+} binding into F-actin–bundling inhibition might be different, as α-actinins of higher eukaryotes display notably lower affinity to Ca^{2+} [K_d of 50 to 100 μM for CaMD of *h*Actn2 (37, 38)] and exhibit an evolved rod domain (four SRs) that in *h*Actn2 shows a closed conformation. This is also likely to occur in Ca^{2+}-regulated isoforms, as inferred from high sequence identity (76 to 79%; *SI Appendix*, Fig. S15), which might lead to a different interaction platform for the CaMD and result in a differently tuned mechanism.

Furthermore, interactions of CaMDs from structurally related cytoskeletal F-actin–binding proteins such as dystrophin, utrophin, and spectrin might play important roles in regulating cytoskeletal interactions near the plasma membrane (53), as suggested by recent studies on spectrin/ankyrin, actin, and protein 4.2 interactions (54, 55). Although the domain composition is different, for example, spectrin forms a tetramer composed of α- and β-spectrin dimers, the general mode of regulation is similar to that of α-actinin, namely the CH2-R1 linker region of α/β-spectrin also binds to CaMD EF3-4, thus regulating protein interactions.

The mechanism we present here is therefore likely to be of general relevance for regulating spectrin-like proteins via an interdomain cross-talk mechanism.

Materials and Methods

All *Eh*Actn2 constructs were produced by recombinant expression in *Escherichia coli* and purified by nickel-affinity chromatography, anion-exchange chromatography, and SEC. Ca^{2+} content and affinity were determined using intact mass spectrometry and low/high-affinity fluorescent dyes. Protein conformation and stability were analyzed by SEC-MALS, CD, SAXS, FA, DLS, and limited proteolysis in the absence and presence of Ca^{2+} and Mg^{2+}. Protein–ion and protein–protein interactions were measured by ITC and F-actin bundling and binding analyzed by cosedimentation and rheology assays. The structures of F-actin–binding and rod domains were determined by molecular replacement and single-wavelength anomalous dispersion, respectively, the structure of tetragonal *Eh*Actn2 by single-wavelength anomalous dispersion, and the structures of orthorhombic

*Eh*Actn2 and ΔCa by molecular replacement. Immunofluorescence staining of trophozoites, preparation of cell lysates for Western blotting, and erythrophagocytosis assays using trophozoites plus RBCs were carried out as detailed in *SI Appendix, Materials and Methods*.

Data Availability. The atomic coordinates of the structures reported in this paper have been deposited in the Protein Data Bank, https://www.wwpdb.org/ (PDB ID codes 5NL6, 5NL7, 6SL2, 6SL3, and 6SL7). All other relevant data are described in *SI Appendix* or are available upon request. Full methods can be found in *SI Appendix, Materials and Methods*.

All study data are included in the article and *SI Appendix*.

ACKNOWLEDGMENTS. We thank the staff of the macromolecular crystallography (MX) and SAXS beamlines at the European Synchrotron Radiation facility, Diamond, and Swiss Light Source for excellent support, and the Life Sciences Facility of the Institute of Science and Technology Austria for usage of the rheometer. We thank Life Sciences editors for editing assistance. EM data were recorded at the EM Facility of the Vienna BioCenter Core Facilities (Austria). Confocal microscopy was carried out at the Advanced Instrument Research Facility, Jawaharlal Nehru University. K.D.-C.'s research was supported by the Initial Training Network MUZIC (ITN-MUZIC) (N°238423), Austrian Science Fund (FWF) Projects I525, I1593, P22276, P19060, and W1221, Laura Bassi Centre of Optimized Structural Studies (N°253275), a Wellcome Trust Collaborative Award (201543/Z/16/Z), COST Action BM1405, Vienna Science and Technology Fund (WWTF) Chemical Biology Project LS17-008, and Christian Doppler Laboratory for High-Content Structural Biology and Biotechnology. K.Z., J.L.A., C.S., E.A.G., and A.S. were supported by the University of Vienna, J.K. by a Wellcome Trust Collaborative Award and by the Centre of Optimized Structural Studies, M.P. by FWF Project I1593, E.d.A.R. ITN-MUZIC, and FWF Projects I525 and I1593, and T.C.M. and L.C. by FWF Project I 2408-B22. E.A.G. acknowledges the PhD program Structure and Interaction of Biological Macromolecules. M.B. acknowledges the University Grant Commission, India, for a senior research fellowship. A.B. acknowledges a JC Bose Fellowship from the Science Engineering Research Council.

1. K. Djinovic-Carugo, M. Gautel, J. Ylänne, P. Young, The spectrin repeat: A structural platform for cytoskeletal protein assemblies. *FEBS Lett.* **513**, 119–123 (2002).
2. B. Sjöblom, A. Salmazo, K. Djinović-Carugo, Alpha-actinin structure and regulation. *Cell. Mol. Life Sci.* **65**, 2688–2701 (2008).
3. K. Fukami *et al*., Requirement of phosphatidylinositol 4,5-bisphosphate for α-actinin function. *Nature* **359**, 150–152 (1992).
4. E. d. A. Ribeiro, Jr *et al*., The structure and regulation of human muscle α-actinin. *Cell* **159**, 1447–1460 (2014).
5. P. Young, M. Gautel, The interaction of titin and α-actinin is controlled by a phospholipid-regulated intramolecular pseudoligand mechanism. *EMBO J.* **19**, 6331–6340 (2000).
6. K. S. Foley, P. W. Young, The non-muscle functions of actinins: An update. *Biochem. J.* **459**, 1–13 (2014).
7. C. A. Otey, O. Carpen, Alpha-actinin revisited: A fresh look at an old player. *Cell Motil. Cytoskeleton* **58**, 104–111 (2004).
8. J. R. Bartles, Parallel actin bundles and their multiple actin-bundling proteins. *Curr. Opin. Cell Biol.* **12**, 72–78 (2000).
9. F. Landon, Y. Gache, H. Touitou, A. Olomucki, Properties of two isoforms of human blood platelet alpha-actinin. *Eur. J. Biochem.* **153**, 231–237 (1985).
10. K. Burridge, J. R. Feramisco, Non-muscle alpha actinins are calcium-sensitive actin-binding proteins. *Nature* **294**, 565–567 (1981).
11. M. Pacaud, M. C. Harricane, Macrophage alpha-actinin is not a calcium-modulated actin-binding protein. *Biochemistry* **32**, 363–374 (1993).
12. A. Virel, L. Backman, Molecular evolution and structure of alpha-actinin. *Mol. Biol. Evol.* **21**, 1024–1031 (2004).
13. A. Virel, L. Backman, A comparative and phylogenetic analysis of the alpha-actinin rod domain. *Mol. Biol. Evol.* **24**, 2254–2265 (2007).
14. S. L. Stanley, Jr, Amoebiasis. *Lancet* **361**, 1025–1034 (2003).
15. W. Stauffer, J. I. Ravdin, *Entamoeba histolytica*: An update. *Curr. Opin. Infect. Dis.* **16**, 479–485 (2003).
16. G. B. Bailey, D. B. Day, J. W. Gasque, Rapid polymerization of *Entamoeba histolytica* actin induced by interaction with target cells. *J. Exp. Med.* **162**, 546–558 (1985).
17. G. B. Bailey, D. B. Day, C. Nokkaew, C. C. Harper, Stimulation by target cell membrane lipid of actin polymerization and phagocytosis by *Entamoeba histolytica*. *Infect. Immun.* **55**, 1848–1853 (1987).
18. H. Voigt, N. Guillén, New insights into the role of the cytoskeleton in phagocytosis of *Entamoeba histolytica*. *Cell. Microbiol.* **1**, 195–203 (1999).
19. K. Tejle, K. E. Magnusson, B. Rasmusson, Phagocytosis and phagosome maturation are regulated by calcium in J774 macrophages interacting with unopsonized prey. *Biosci. Rep.* **22**, 529–540 (2002).
20. J. I. Ravdin, F. Moreau, J. A. Sullivan, W. A. Petri, Jr, G. L. Mandell, Relationship of free intracellular calcium to the cytolytic activity of *Entamoeba histolytica*. *Infect. Immun.* **56**, 1505–1512 (1988).
21. R. Jain *et al*., Calcium-binding protein 1 of *Entamoeba histolytica* transiently associates with phagocytic cups in a calcium-independent manner. *Cell. Microbiol.* **10**, 1373–1389 (2008).
22. M. Babuta, S. Kumar, S. Gourinath, S. Bhattacharya, A. Bhattacharya, Calcium-binding protein *Eh*CaBP3 is recruited to the phagocytic complex of *Entamoeba histolytica* by interacting with Arp2/3 complex subunit 2. *Cell. Microbiol.* **20**, e12942 (2018).
23. N. Kumar *et al*., *Eh*Coactosin stabilizes actin filaments in the protist parasite *Entamoeba histolytica*. *PLoS Pathog.* **10**, e1004362 (2014).
24. J. Ylänne, K. Scheffzek, P. Young, M. Saraste, Crystal structure of the alpha-actinin rod reveals an extensive torsional twist. *Structure* **9**, 597–604 (2001).
25. B. Mohapatra *et al*., Mutations in the muscle LIM protein and alpha-actinin-2 genes in dilated cardiomyopathy and endocardial fibroelastosis. *Mol. Genet. Metab.* **80**, 207–215 (2003).
26. A. W. Avery *et al*., Structural basis for high-affinity actin binding revealed by a β-III-spectrin SCA5 missense mutation. *Nat. Commun.* **8**, 1350 (2017).
27. D. V. Iwamoto *et al*., Structural basis of the filamin A actin-binding domain interaction with F-actin. *Nat. Struct. Mol. Biol.* **25**, 918–927 (2018).
28. V. E. Galkin, A. Orlova, A. Salmazo, K. Djinović-Carugo, E. H. Egelman, Opening of tandem calponin homology domains regulates their affinity for F-actin. *Nat. Struct. Mol. Biol.* **17**, 614–616 (2010).
29. E. Krissinel, K. Henrick, Inference of macromolecular assemblies from crystalline state. *J. Mol. Biol.* **372**, 774–797 (2007).
30. G. Karlsson, C. Persson, M. Mayzel, M. Hedenström, L. Backman, Solution structure of the calmodulin-like C-terminal domain of *Entamoeba* α-actinin2. *Proteins* **84**, 461–466 (2016).
31. A. Virel, B. Addario, L. Backman, Characterization of *Entamoeba histolytica* alpha-actinin2. *Mol. Biochem. Parasitol.* **154**, 82–89 (2007).
32. O. Carugo, P. Argos, NADP-dependent enzymes. II: Evolution of the mono- and di-nucleotide binding domains. *Proteins* **28**, 29–40 (1997).
33. A. Houdusse *et al*., Crystal structure of apo-calmodulin bound to the first two IQ motifs of myosin V reveals essential recognition features. *Proc. Natl. Acad. Sci. U.S.A.* **103**, 19326–19331 (2006).
34. K. M. Trybus *et al*., Effect of calcium on calmodulin bound to the IQ motifs of myosin V. *J. Biol. Chem.* **282**, 23316–23325 (2007).
35. R. A. Atkinson *et al*., Ca^{2+}-independent binding of an EF-hand domain to a novel motif in the alpha-actinin-titin complex. *Nat. Struct. Biol.* **8**, 853–857 (2001).
36. R. E. Reid, Synthetic fragments of calmodulin calcium-binding site III. A test of the acid pair hypothesis. *J. Biol. Chem.* **265**, 5971–5976 (1990).
37. L. Backman, Calcium affinity of human α-actinin 1. *PeerJ* **3**, e944 (2015).
38. S. Drmota Prebil *et al*., Structure and calcium-binding studies of calmodulin-like domain of human non-muscle α-actinin-1. *Sci. Rep.* **6**, 27383 (2016).
39. J. L. Gifford, M. P. Walsh, H. J. Vogel, Structures and metal-ion-binding properties of the Ca^{2+}-binding helix-loop-helix EF-hand motifs. *Biochem. J.* **405**, 199–221 (2007).
40. A. Romani, A. Scarpa, Regulation of cell magnesium. *Arch. Biochem. Biophys.* **298**, 1–12 (1992).
41. M. R. Nelson, W. J. Chazin, An interaction-based analysis of calcium-induced conformational changes in Ca^{2+} sensor proteins. *Protein Sci.* **7**, 270–282 (1998).
42. A. Blanchard, V. Ohanian, D. Critchley, The structure and function of alpha-actinin. *J. Muscle Res. Cell Motil.* **10**, 280–289 (1989).
43. K. P. Hoeflich, M. Ikura, Calmodulin in action: Diversity in target recognition and activation mechanisms. *Cell* **108**, 739–742 (2002).
44. P. M. Bayley, W. A. Findlay, S. R. Martin, Target recognition by calmodulin: Dissecting the kinetics and affinity of interaction using short peptide sequences. *Protein Sci.* **5**, 1215–1228 (1996).
45. D. H. Wachsstock, W. H. Schwarz, T. D. Pollard, Cross-linker dynamics determine the mechanical properties of actin gels. *Biophys. J.* **66**, 801–809 (1994).
46. M. Sato, W. H. Schwarz, T. D. Pollard, Dependence of the mechanical properties of actin/alpha-actinin gels on deformation rate. *Nature* **325**, 828–830 (1987).
47. D. H. Wachsstock, W. H. Schwartz, T. D. Pollard, Affinity of alpha-actinin for actin determines the structure and mechanical properties of actin filament gels. *Biophys. J.* **65**, 205–214 (1993).
48. M. Sato, G. Leimbach, W. H. Schwarz, T. D. Pollard, Mechanical properties of actin. *J. Biol. Chem.* **260**, 8585–8592 (1985).
49. S. Marion, P. Tavares, P. Arhets, N. Guillén, Signal transduction through the Gal-GalNAc lectin of *Entamoeba histolytica* involves a spectrin-like protein. *Mol. Biochem. Parasitol.* **135**, 31–38 (2004).
50. D. Sehgal, A. Bhattacharya, S. Bhattacharya,Pathogenesis of infection by *Entamoeba histolytica*. *J. Biosci.* **21**, 423–432 (1996).
51. K. Kwiatkowska, A. Sobota, Local accumulation of α-spectrin-related protein under plasma membrane during capping and phagocytosis in *Acanthamoeba*. *Cell Motil. Cytoskeleton* **36**, 253–265 (1997).
52. D. T. Shirley, L. Farr, K. Watanabe, S. Moonah, A review of the global burden, new diagnostics, and current therapeutics for amebiasis. *Open Forum Infect. Dis.* **5**, ofy161 (2018).
53. V. Bennett, J. Healy, Organizing the fluid membrane bilayer: Diseases linked to spectrin and ankyrin. *Trends Mol. Med.* **14**, 28–36 (2008).
54. C. Korsgren, L. L. Peters, S. E. Lux, Protein 4.2 binds to the carboxyl-terminal EF-hands of erythroid alpha-spectrin in a calcium- and calmodulin-dependent manner. *J. Biol. Chem.* **285**, 4757–4770 (2010).
55. C. Korsgren, S. E. Lux, The carboxyterminal EF domain of erythroid alpha-spectrin is necessary for optimal spectrin-actin binding. *Blood* **116**, 2600–2607 (2010).